



HST*/COS Observations of Quasar Outflows in the 500–1050 Å Rest Frame. III. Four Similar Outflows in 2MASS J1051+1247 with Enough Energy to Be Major Contributors to AGN Feedback

Timothy R. Miller¹ , Nahum Arav¹ , Xinfeng Xu¹ , Gerard A. Kriss² , and Rachel J. Plesha²

¹Department of Physics, Virginia Polytechnic Institute and State University, Blacksburg, VA 24061, USA

²Space Telescope Science Institute, 3700 San Martin Drive, Baltimore, MD 21218, USA

Received 2019 June 27; revised 2019 September 24; accepted 2019 October 2; published 2020 March 16

Abstract

We detect four very energetic outflows in the *Hubble Space Telescope*/Cosmic Origins Spectrograph spectra of quasar 2MASS J1051+1247 with a combined kinetic luminosity (\dot{E}_K) of 10^{46} erg s^{−1}. Remarkable similarities are seen in these outflows: velocity centroids between 4900 and 5700 km s^{−1}, distances from the central source (R) of a few hundred parsecs that are all consistent within the errors, and an \dot{E}_K within a factor of two for all outflows. Hence, a common origin for the outflows is probable. Most of the outflowing mass resides in a very high-ionization phase evident by troughs from Ne VIII, Na IX, Mg X, and Si XII, which connect the physical conditions of these ultraviolet outflows to the X-ray warm absorber outflows seen in nearby Seyfert galaxies. Three of the outflows have two or three independent diagnostics for the electron number density, yielding consistent values for each outflow, which increase the robustness of the R determinations. Troughs from never-before-seen ionic transitions of Ar VI, O IV*, Ne VI*, and Ne V* are identified. With a combined \dot{E}_K that is $7.0^{+6.5}_{-2.3}\%$ of the quasar’s Eddington luminosity, these outflows are prime candidates to be major agents for various active galactic nuclei feedback effects.

Unified Astronomy Thesaurus concepts: Active galactic nuclei (16); Quasars (1319); Active galaxies (17); AGN host galaxies (2017); Broad-absorption line quasar (183); Quasar absorption line spectroscopy (1317)

1. Introduction

Blueshifted absorption troughs in the rest frame of quasar spectra are used to identify outflowing material from the host galaxy. A large fraction (up to 40%; Hewett & Foltz 2003; Dai et al. 2008; Ganguly & Brotherton 2008; Knigge et al. 2008) of the quasar population shows absorption outflows. Many feedback processes seen in active galactic nuclei (AGN) are likely caused by these outflows (see elaboration in Section 1 of Arav et al. 2020, hereafter Paper I, and references therein).

The potential for these outflow systems to produce the aforementioned feedback rests primarily on their kinetic luminosity (\dot{E}_K), which is linearly dependent on the distance from the central source (R). Simultaneously determining the electron number density (n_e) and ionization parameter (U_H) of the outflow is the most robust way to infer these distances (see Section 7.1 of Arav et al. 2018). Our group and others have used this method to publish around 20 such distances (see Section 1 of Paper I and references therein). The range for these distances is between parsecs to tens of kiloparsecs and is orders of magnitude larger than theoretical predictions (accretion disk wind models predict ~ 0.03 pc; e.g., Murray et al. 1995; Proga et al. 2000; Proga & Kallman 2004).

The ratio of the kinetic luminosity with respect to the Eddington luminosity is used to judge the feedback potential. Ratios exceeding 0.5% (Hopkins & Elvis 2010), or 5% (Scannapieco & Oh 2004), are thought to be sufficient. There are six known outflow systems that meet at least one of these

criteria (Moe et al. 2009; Arav et al. 2013; Borguet et al. 2013; Chamberlain & Arav 2015; Xu et al. 2019).

The observations analyzed here were taken during Cycle 24 (GO-14777, PI: N. Arav) as part of a spectroscopic survey of 10 quasars with known outflows and redshifts around 1. The goal was to probe the 500–1050 Å rest-frame wavelength range (EUV500) for numerous diagnostic troughs like those listed in Arav et al. (2013) that can yield n_e and also troughs that arise from very high-ionization potential ions (e.g., Ne VIII, Mg X, and Si XII) that are typically seen in X-ray warm absorbers (e.g., Reynolds 1997; Kaastra et al. 2000; Crenshaw et al. 2003; Kaastra et al. 2014). With these very high-ionization potential ions, a connection can be established between X-ray warm absorbers and ultraviolet (UV) AGN outflows (Arav et al. 2013).

This paper is part of a series of publications describing the results of *Hubble Space Telescope* (HST) program GO-14777.

Paper I summarizes the results for the individual objects, and discusses their importance to various aspects of quasar outflow research.

Paper II (Xu et al. 2020a) gives the full analysis for four outflows detected in SDSS J1042+1646, including the largest \dot{E}_K (10^{47} erg s^{−1}) outflow measured to date at $R = 800$ pc, and an outflow at $R = 15$ pc.

Paper III is this work.

Paper IV (Xu et al. 2020b) presents the largest velocity shift and acceleration measured to date in a broad absorption line (BAL) outflow.

Paper V (Miller et al. 2020) analyzes two outflows detected in PKS J0352-0711, including one outflow at $R = 500$ pc and a second outflow at $R = 10$ pc that shows an ionization potential-dependent velocity shift for troughs from different ions.

* Based on observations with the NASA/ESA *Hubble Space Telescope* obtained at the Space Telescope Science Institute, which is operated by the Association of Universities for Research in Astronomy, Incorporated, under NASA contract NAS5-26555.

Table 1
HST/COS Observations from 2013 to 2018 for 2MASS J1051+1247

	Date		
	2013 May 17	2018 Jan 4	2018 Jan 4
<i>HST</i> /COS grating	G130M	G130M	G160M
Exposure time (s)	10,869	3460	4640
Observed range (Å)	1145–1470	1130–1470	1405–1800
Rest-frame range (Å)	500–645	495–645	615–790

Paper VI (Xu et al. 2020c) analyzes two outflows detected in SDSS J0755+2306, including one at $R = 220$ pc with $\dot{E}_k = 10^{46}$ erg s $^{-1}$.

Paper VII (T. R. Miller et al. 2020, in preparation) discusses the other objects observed by program GO-14777, whose outflow characteristics make the analysis more challenging.

The structure of this paper is as follows. Section 2 describes the new observations of 2MASS J10512569+1247462 (hereafter, 2MASS J1051+1247) taken by the *HST*/Cosmic Origins Spectrograph (COS; Green et al. 2012). The spectral fitting for the unabsorbed continuum and emission lines is also discussed. Determinations of the ionic column densities and electron number densities as well as the photoionization modeling are in Section 3. Section 4 presents our results on the physical properties, distances, and energetics of each outflow followed by a discussion in Section 5. Section 6 closes with a summary and conclusions. Throughout this paper, we adopt a cosmology of $h = 0.696$, $\Omega_m = 0.286$, and $\Omega_\Lambda = 0.714$ and use Ned Wright’s Javascript Cosmology Calculator website (Wright 2006).

2. Observations, Data Reduction, and Spectral Fitting

2MASS J1051+1247 (J2000: R.A. = 10:51:25.69, decl. = +12:47:46.2, $z = 1.2828$) was first observed by *HST*/COS in 2013 May (PID 12603) and again in 2018 January (PID 14777). Table 1 contains the details of each observation. Both data sets were processed in the same way as described in Miller et al. (2018) and were corrected for Galactic extinction with $E(B-V) = 0.0202$ (Schlafly & Finkbeiner 2011). Figure 1 shows the dereddened, one-dimensional spectra in black and purple with errors in gray and light red for the 2013 and 2018 epochs, respectively. Absorption troughs for the four outflow systems are delineated S1, S2, S3, and S4 with centroid velocities and widths summarized in Table 2. All four outflows contain at least one previously undetected absorption trough: Ar VI 544.73 Å and 548.90 Å, O IV* 555.26 Å, Ne VI* 562.80 Å, and Ne V* 569.83 Å and 572.34 Å. Intervening hydrogen absorption systems are marked with slanted, dark green lines. The labels B1–B10 are the following blended troughs: B1 = O IV 553 S2, O IV 553 S3, and O IV 554 S4; B2 = O IV 553 S1, O IV 554 S3, and O IV* 554.5 S4; B3 = O IV 554 S2 and O IV* 554.5 S3; B4 = O IV 554 S1, O IV* 554.5 S2, and O IV* 555 S4; B5 = O IV* 554.5 S1 and O IV* 555 S3; B6 = Ne V 568 S1 and Ne V* 570 S4; B7 = O IV 608 S1, Mg X 610 S4, and O IV* 610 S4; B8 = Mg X 610 S3 and O IV* 610 S3; B9 = Mg X 610 S2 and O IV* 610 S2; B10 = Mg X 610 S1 and O IV* 610 S1.

Following the methodology of Miller et al. (2018), the continuum emission was fitted with a power law, and line emission features were modeled with Gaussian profiles. The

Gaussian fits were constrained by the red side of each line, avoiding the absorption that occurs mostly on the blue side of any given emission line. The Gaussian centroids were fixed at the rest-frame wavelength of each emission line. The solid red contour in Figure 1 shows the unabsorbed emission model adopted in this work for the 2013 epoch up to 645 Å (rest frame) and the 2018 epoch at larger wavelengths.

3. Data Analysis

3.1. Ionic Column Density

As detailed in Miller et al. (2018), the apparent optical depth (AOD) and partial covering (PC) methods were used to measure ionic column densities (N_{ion}). The AOD method uses one ionic transition, while the PC method uses two ionic transitions to determine a single N_{ion} for each ionic energy state. The PC method is applicable when multiple lines (with different oscillator strengths, f) from the same ionic energy state have different trough depths, yielding a viable partial covering solution. Upon visual inspection, the troughs within the normalized spectra from each epoch did not show significant variability. Therefore, we used the column density measurements from the 2013 epoch when possible since the signal to noise is larger.

The sum of all ionic energy state N_{ion} yields the total column density of each ion as listed in Table 3 for all outflows. Upper and lower limits are highlighted in italics and bold, respectively. S1 has an upper and lower limit N_{ion} for Ar VI. The total N_{ion} for Ar VI is the sum of the column densities for the resonance and excited states. The lower limit is obtained from the Ar VI 548.90 and 544.73 Å resonance troughs using the PC method without the addition of the excited state N_{ion} . The Ar VI* 551.36 Å trough is contaminated with unidentified absorption, so only an upper limit for Ar VI* can be obtained from the Ar VI* 596.67 Å region ($85^{+30} \times 10^{12}$ cm $^{-2}$), yielding an overall upper limit to the total N_{ion} for Ar VI as listed in the table. The last column contains the ratio of the adopted column densities to the best-fit, model predicted column densities (see Section 3.2 and Figure 2). This ratio is expected to be less than one for measured N_{ion} lower limits and vice versa for upper limits. The trough labels in Figure 1 combine multiple transitions with wavelength separations less than 0.5 Å into a single transition. Table 3 of Paper II provides a list of transition atomic data.

Using the same criteria of Paper II to account for non-black saturation, all PC determined N_{ion} are treated as measurements, N_{ion} measured for regions where no trough is identified (maximum optical depth, τ_{max} , less than 0.05) are upper limits, and N_{ion} from troughs where both $0.05 < \tau_{\text{max}} < 0.5$ and troughs from ions of similar ionization potential that have $\tau_{\text{max}} > 2$ are also treated as measurements. Our adopted values are the PC values when available and AOD values otherwise. A systematic error, 20% of the adopted value, is added in quadrature with the corresponding AOD/PC errors, yielding the adopted error values (see Table 3). This systematic error accounts for uncertainties in the unabsorbed emission model (e.g., Miller et al. 2018; Xu et al. 2018). For example, N IV of S1 has an AOD $N_{\text{ion}} = 310^{+70}_{-40}$. Since we are treating the adopted value as a lower limit, we calculate the lower error as $\sqrt{(40)^2 + (0.2 * 310)^2} \approx 70$.

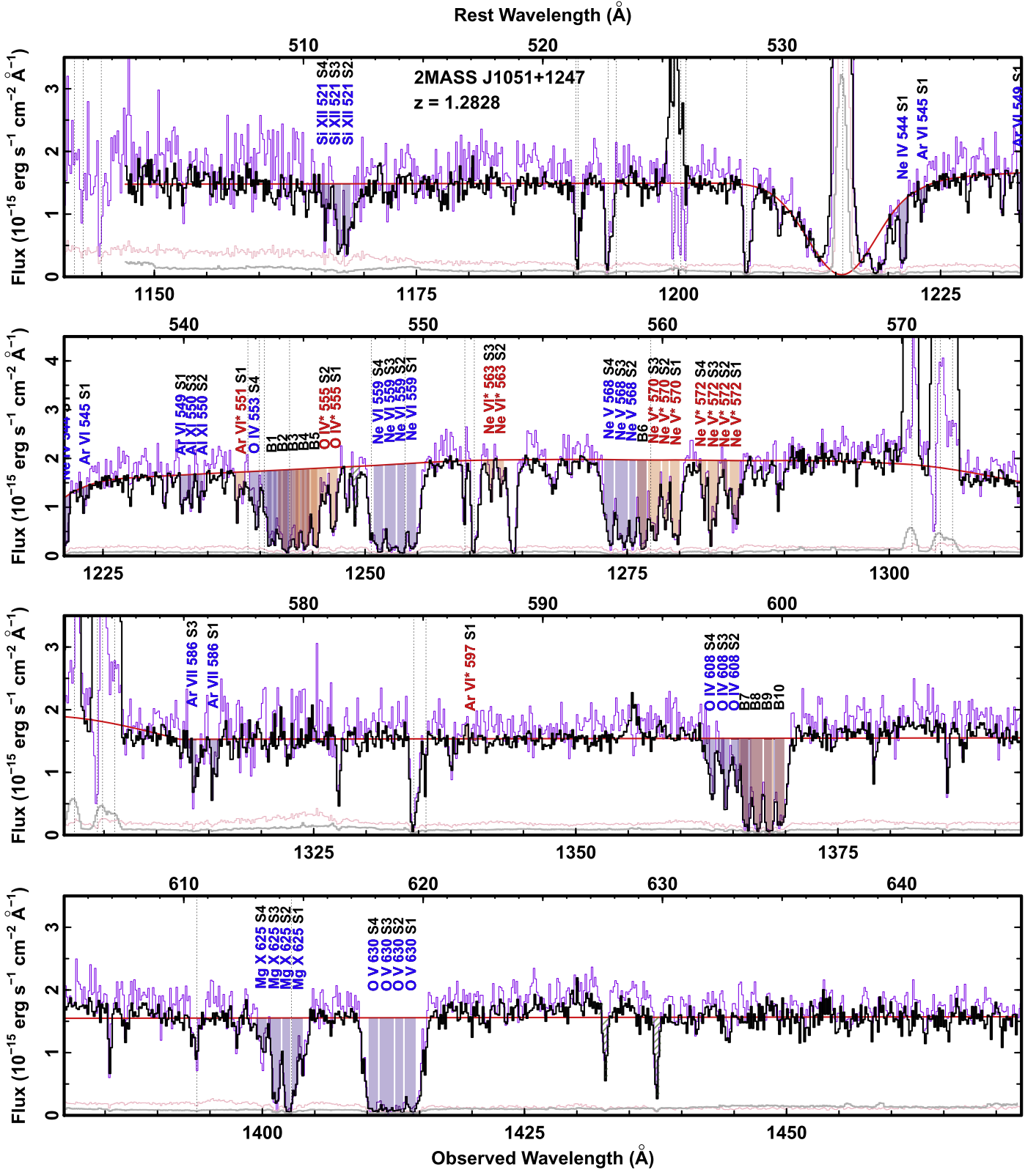


Figure 1. Dereddened 2013 *HST*/COS spectrum (in black) with errors (in gray) along with the dereddened 2018 spectrum (in purple) and errors (in light red). The main absorption troughs are labeled for all outflow systems (S1 = -4900 km s^{-1} , S2 = -5150 km s^{-1} , S3 = -5350 km s^{-1} , S4 = -5650 km s^{-1}). Identifications for transitions yielding upper limits are excluded, except for Ar VI* 597 of S1 (see Section 3.1). Blue shaded regions mark transitions from resonance absorption lines, and red regions mark excited ones. Blended troughs (B1–B10) are also labeled (see Section 2). Absorption troughs from intervening systems are the slanted dark green shaded regions, and the vertical dashed lines mark Galactic absorption and geocoronal emission features. The red contour traces the unabsorbed emission model for the 2013 data up to 645 \AA (rest frame) and the 2018 data at larger wavelengths.

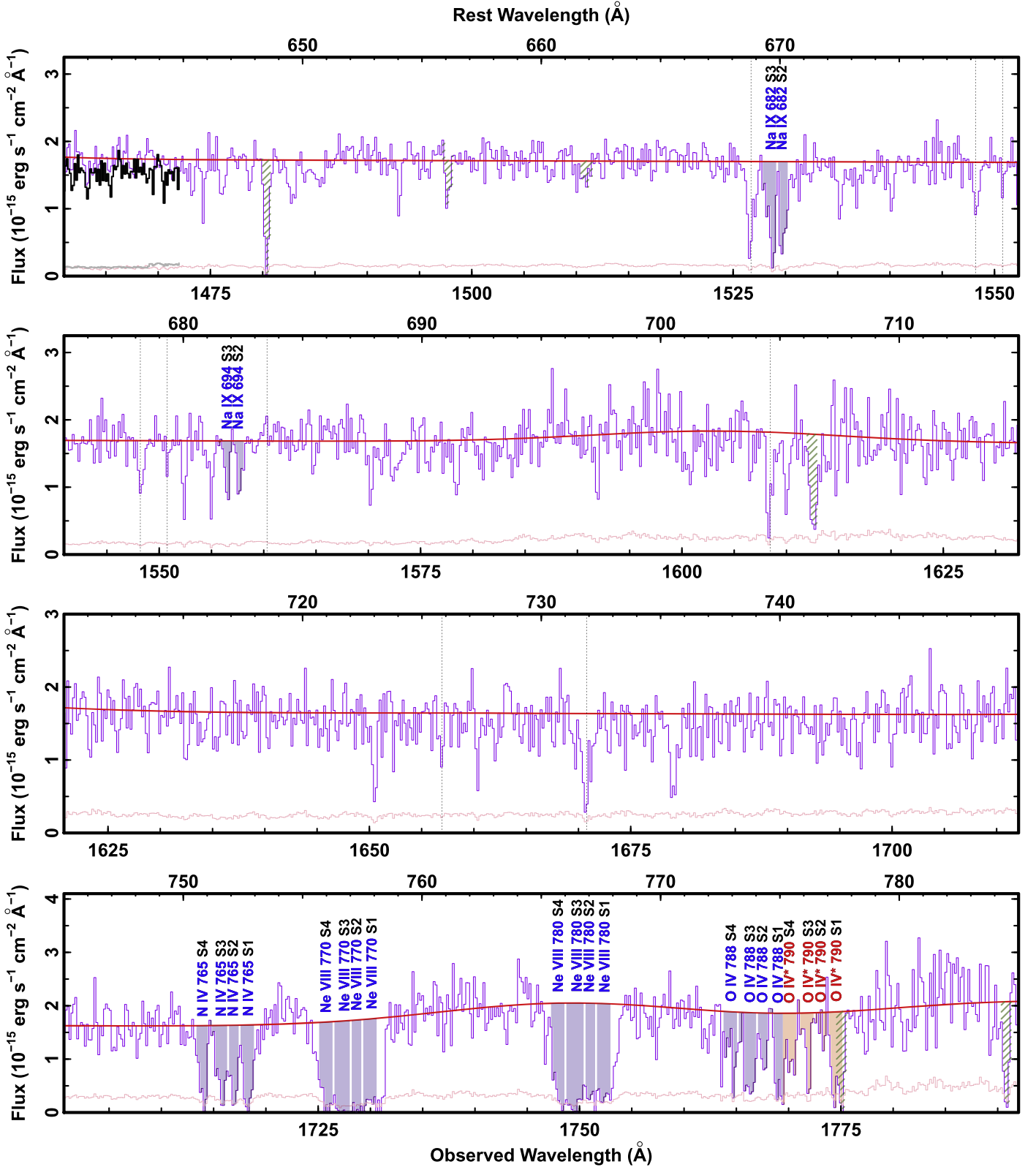


Figure 1. (Continued.)

3.2. Photoionization Modeling

Since the troughs in each outflow are narrow and the blended troughs are not critical to the analysis, we do not use the Synthetic Spectral Simulation (SSS) method presented in

Paper II and instead follow the methodology of prior works (e.g., Miller et al. 2018; Xu et al. 2018, 2019). Each outflow system is modeled with a hydrogen column density (N_{H}) and U_{H} . We generated grids of photoionization models with the

Table 2
Detected Outflows in 2MASS J1051+1247

Outflow System	Centroid Velocity (km s ⁻¹)	FWHM (km s ⁻¹)
S1	-4900	250
S2	-5150	200
S3	-5350	300
S4	-5650	250

code Cloudy (Ferland et al. 2017, version c17.00). Each grid assumed one metallicity (two total) and one spectral energy distribution (SED, three total). The three SEDs are the UV-soft SED (Dunn et al. 2010), the HE0238 SED (Arav et al. 2013), and the MF87 SED (Mathews & Ferland 1987), of which are a representative range of SED shapes that are applicable for radio-quiet quasars (Arav et al. 2013). The two metallicities are solar, Z_{\odot} , from Grevesse et al. (2010) and super-solar, $Z = 4.68Z_{\odot}$, from Paper V. These parameters directly determine the model N_{ion} .

To determine the best pair of N_{H} and U_{H} , the measured N_{ion} are compared to the modeled values. The colored contours for individual ions in Figure 2 show the N_{H} and U_{H} pairs where the model N_{ion} are within 1σ of the observed values, assuming the HE0238 SED and the solar metallicity. Solid contours represent N_{ion} measurements while dotted and dashed lines indicate upper and lower limits, respectively. χ^2 -minimization of the model N_{ion} compared to the measured N_{ion} from Table 3 determines the best-fit solution. The adopted, best-fit solution is the HE0238 SED with the solar metallicity (solid black dots and 1σ error ellipses). Assuming the solar metallicity and changing the SED results in the solid red (UV-soft SED) and solid green (MF87 SED) solutions. As expected, the N_{ion} contours shift according to the SED shape. For example, the UV-soft SED has a higher luminosity at the wavelengths needed to produce the high- and very high-ionization potential ions, resulting in a lower-ionization parameter in both phases. Similarly, assuming the super-solar metallicity decreases the hydrogen column density required to match the observations, and the associated solutions for each SED are the plus symbols with dashed ellipses.

A two-phase photoionization solution (Arav et al. 2013) is needed for all outflow systems to satisfy the column density measurements from both the very high-ionization potential ions (e.g., Mg X, Na IX, and Al XI) and high-ionization potential ions (e.g., Ne IV, Ne V, and O IV). For S1, a single phase solution at the intersection of the Ne IV and Na IX contours over predicts the upper limit column densities of Ca VI, Ca VIII, and Ar VIII by over an order of magnitude. Similar over predictions occur for the other outflow systems when a single phase solution is chosen. The values for all N_{H} and U_{H} determinations are given in Table 4.

3.3. Electron Number Density Determination

The excited state troughs shown in Figure 1 all become populated through electron collisions. The frequency of collisions and amount of energy transferred between bound and free electrons depend on n_e and the electron temperature. Therefore, n_e can be calculated from the relative populations between either two different excited states or an excited state and a resonance state from the same ion (e.g., de Kool et al. 2001, 2002;

Table 3
Total Ionic Column Densities

Ion	AOD ^a (10 ¹² cm ⁻²)	PC ^a (10 ¹² cm ⁻²)	Adopted ^b (10 ¹² cm ⁻²)	Adopted ^c Best Model
$v = -4900 \text{ km s}^{-1}$				
N IV	310 ⁺⁷⁰ ₋₄₀	...	>310-70	>0.23-0.05
O III	520 ⁺⁹⁰ ₋₇₀	...	<520 ⁺¹⁵⁰	<3.07 ^{+0.89}
O IV	3100 ⁺⁸³⁰ ₋₂₈₀	...	>3100-670	>0.30-0.07
O V	820 ⁺⁶⁰ ₋₄₀	...	>820-170	>0.02-0.004
Ne IV	980 ⁺⁵⁰ ₋₅₀	...	>980-200	>1.00-0.21
Ne V	5900 ⁺¹⁴⁰ ₋₇₀	...	>5900-1160	>0.72-0.14
Ne VI	3900 ⁺¹³⁰ ₋₁₁₀	...	>3900-790	>0.23-0.05
Ne VIII	4600 ⁺⁷⁷⁰ ₋₄₇₀	...	>4600-1100	>0.20-0.04
Na IX	240 ⁺¹¹⁰ ₋₁₁₀	...	<240 ⁺¹²⁰	<0.98 ^{+0.49}
Mg X	3300 ⁺¹⁵⁰ ₋₁₄₀	...	>3300-670	>0.94-0.19
Al XI	170 ⁺⁵⁰ ₋₅₀	...	<170 ⁺⁵⁰	<3.36 ^{+0.99}
Si XII	1600 ⁺²³⁰ ₋₁₈₀	...	<1600 ⁺⁴¹⁰	<26.77 ^{+6.44}
S IV	25 ⁺⁴ ₋₄	...	<25 ⁺⁷	<1.00 ^{+0.28}
Cl VI	9.5 ^{+4.2} _{-3.5}	...	<9.5 ^{+4.6}	<1.07 ^{+0.52}
Ar VI	130 ⁺²⁰ ₋₂₀	160 ⁺²⁰ ₋₂₀	>160-40	>0.88-0.22
Ar VI	<250 ⁺⁷⁰	<1.37 ^{+0.38}
Ar VII	44 ⁺⁴ ₋₃	...	>44-9	>1.04-0.21
Ar VIII	120 ⁺⁴⁰ ₋₃₀	...	<120 ⁺⁵⁰	<1.73 ^{+0.72}
Ca VI	180 ⁺⁸⁰ ₋₆₀	...	<180 ⁺⁹⁰	<0.91 ^{+0.45}
Ca VIII	130 ⁺⁵⁰ ₋₄₀	...	<130 ⁺⁵⁰	<0.95 ^{+0.36}
$v = -5150 \text{ km s}^{-1}$				
N IV	210 ⁺⁸⁰ ₋₃₀	...	>210-50	>0.53-0.13
O III	250 ⁺⁶⁰ ₋₅₀	...	<250 ⁺¹⁰⁰	<6.69 ^{+2.68}
O IV	1400 ⁺¹⁰⁰ ₋₁₇₀	...	>1400-350	>0.45-0.10
O V	810 ⁺²¹⁰ ₋₄₀	...	>810-170	>0.06-0.01
Ne IV	270 ⁺³⁰ ₋₃₀	...	<270 ⁺⁶⁰	<0.95 ^{+0.21}
Ne V	3500 ⁺¹¹⁰ ₋₄₀	...	>3500-680	>1.16-0.23
Ne VI	5100 ⁺²³⁰ ₋₂₀₀	...	>5100-1100	>0.82-0.17
Ne VIII	4200 ⁺¹⁰⁰⁰ ₋₄₂₀	...	>4200-930	>0.16-0.04
Na IX	800 ⁺¹⁴⁰ ₋₁₂₀	970 ⁺⁸⁰ ₋₈₀	970 ⁺²¹⁰ ₋₂₁₀	1.15 ^{+0.25} _{-0.25}
Mg X	7700 ⁺⁷⁴⁰ ₋₅₁₀	...	>7700-1600	>0.40-0.08
Al XI	590 ⁺⁴⁰ ₋₄₀	...	590 ⁺¹³⁰ ₋₁₃₀	0.76 ^{+0.17} _{-0.17}
Si XII	3800 ⁺³¹⁰ ₋₂₁₀	...	>3800-770	>1.21-0.25
S IV	7.2 ^{+2.0} _{-3.4}	...	<7.2 ^{+2.4}	<1.35 ^{+0.45}
Cl VI	7.9 ^{+2.8} _{-3.6}	...	<7.9 ^{+3.2}	<2.59 ^{+1.05}
Ar VI	90 ⁺¹⁰ ₋₁₀	...	<90 ⁺²⁰	<1.19 ^{+0.26}
Ar VII	17 ⁺³ ₋₃	...	<17 ⁺⁵	<0.89 ^{+0.26}
Ar VIII	65 ⁺³⁰ ₋₂₀	...	<65 ⁺⁴⁰	<2.26 ^{+1.39}
Ca VI	180 ⁺⁶⁰ ₋₇₀	...	<180 ⁺⁷⁰	<2.28 ^{+0.89}
Ca VIII	200 ⁺⁴⁰ ₋₄₀	...	<200 ⁺⁶⁰	<8.48 ^{+2.54}
$v = -5350 \text{ km s}^{-1}$				
N IV	250 ⁺⁶⁰ ₋₃₀	...	>250-60	>0.67-0.16
O III	560 ⁺⁸⁰ ₋₈₀	...	<560 ⁺¹⁶⁰	<48.93 ^{+13.98}
O IV	2100 ⁺¹⁷⁰ ₋₂₀₀	...	>2100-480	>0.93-0.20
O V	1000 ⁺¹¹⁰ ₋₄₀	...	>1000-170	>0.04-0.01
Ne V	5800 ⁺¹⁰⁰ ₋₉₀	...	>5800-1200	>1.05-0.21
Ne VI	5600 ⁺¹³⁰ ₋₁₈₀	...	>5600-1200	>0.29-0.06
Ne VIII	7800 ⁺²²⁰⁰ ₋₉₀₀	...	>7800-1800	>0.26-0.06
Na IX	760 ⁺¹³⁰ ₋₁₀₀	1000 ⁺⁸⁰ ₋₉₀	1000 ⁺²²⁰ ₋₂₂₀	1.08 ^{+0.24} _{-0.24}
Mg X	4600 ⁺²³⁰ ₋₁₈₀	...	>4600-930	>0.20-0.04
Al XI	440 ⁺⁴⁰ ₋₄₀	...	440 ⁺¹⁰⁰ ₋₁₀₀	0.62 ^{+0.14} _{-0.14}
Si XII	4400 ⁺²⁷⁰ ₋₃₀₀	...	>4400-950	>1.49-0.31
S IV	35 ⁺⁵ ₋₅	...	<35 ⁺⁹	<24.20 ^{+6.22}

Table 3
(Continued)

Ion	AOD ^a (10^{12}cm^{-2})	PC ^a (10^{12}cm^{-2})	Adopted ^b (10^{12}cm^{-2})	Adopted ^c Best Model
Cl VI	$6.5^{+2.8}_{-2.9}$...	$<6.5^{+3.1}$	$<2.30^{+1.10}$
Ar VI	110^{+10}_{-10}	...	$<110^{+30}$	$<1.04^{+0.28}$
Ar VII	46^{+3}_{-3}	...	$>46_{-10}$	$>0.76_{-0.16}$
Ar VIII	240^{+50}_{-50}	...	$<240^{+70}$	$<1.87^{+0.55}$
Ca VI	150^{+80}_{-60}	...	$<150^{+90}$	$<0.86^{+0.52}$
Ca VIII	260^{+40}_{-90}	...	$<260^{+70}$	$<1.73^{+0.46}$
$v = -5650 \text{ km s}^{-1}$				
N IV	230^{+70}_{-30}	...	$>230_{-60}$	$>0.45_{-0.12}$
O III	300^{+70}_{-60}	...	$<300^{+110}$	$<3.82^{+1.40}$
O IV	1700^{+220}_{-190}	...	$>1700_{-400}$	$>0.41_{-0.09}$
O V	880^{+60}_{-40}	...	$>880_{-180}$	$>0.07_{-0.01}$
Ne V	2700^{+100}_{-40}	...	$>2700_{-520}$	$>1.01_{-0.20}$
Ne VI	4600^{+160}_{-160}	...	$>4600_{-950}$	$>1.11_{-0.23}$
Ne VIII	5000^{+1100}_{-600}	...	$>5000_{-1200}$	$>0.27_{-0.06}$
Na IX	900^{+140}_{-130}	...	$<900^{+220}$	$<1.69^{+0.41}$
Mg X	1000^{+120}_{-80}	...	$>1000_{-210}$	$>0.09_{-0.02}$
Al XI	330^{+50}_{-40}	...	$<330^{+80}$	$<0.80^{+0.20}$
Si XII	1800^{+250}_{-180}	...	$>1800_{-390}$	$>1.23_{-0.28}$
S IV	12^{+4}_{-4}	...	$<12^{+5}$	$<0.98^{+0.41}$
Cl VI	$5.7^{+3.3}_{-2.5}$...	$<5.7^{+3.5}$	$<1.80^{+1.10}$
Ar VI	70^{+10}_{-9}	...	$<70^{+20}$	$<1.21^{+0.34}$
Ar VII	10^{+3}_{-2}	...	$<10^{+3}$	$<0.95^{+0.29}$
Ar VIII	60^{+30}_{-30}	...	$<60^{+30}$	$<4.22^{+2.11}$
Ca VI	190^{+90}_{-90}	...	$<190^{+90}$	$<2.97^{+1.40}$
Ca VIII	430^{+90}_{-180}	...	$<430^{+90}$	$<31.06^{+6.50}$

Notes.^a Sum of all N_{ion} from excited and resonance states for a given ion in each outflow system using the AOD and PC methods.^b The adopted values in bold are lower limits, in italics are upper limits, and in roman are measurements.^c The ratio of the adopted values to the column densities from the best-fit Cloudy model.

Hamann et al. 2001; Korista et al. 2008). We used the CHIANTI 8.0.7 database (Dere et al. 1997; Landi et al. 2013) to calculate the necessary population ratios (equal to the column density ratios) as was done in previous works (e.g., Borguet et al. 2012a; Arav et al. 2013, 2015, 2018; Chamberlain & Arav 2015).

However, some of the observed excited states cannot be used with this method. For each outflow system, the O IV* 790.20 Å and 555.26 Å troughs (different $f \cdot \lambda$) exhibit 1:1 trough depths (indicative of non-black saturation) with not only each other but also with the resonance transitions, making column density measurements lower limits for every trough. Therefore, the ratios are unconstrained.

This leaves the Ne VI* 562.81 Å and Ne V* 569.83 Å and 572.34 Å excited troughs with the Ne VI 558.60 Å and Ne V 568.42 Å resonance troughs as potentially useful density diagnostics. Since Ne VI 558.60 Å and Ne V 568.42 Å are the only resonance transitions for each ion and, therefore, yield lower limit measurements, we use the photoionization solutions to constrain the total column densities for these ions. Nearly all of the Ne V column density in each outflow is produced by their respective high-ionization phases. Therefore, an upper limit to the N_{ion} for Ne V is determined by

finding the largest N_{ion} value contained within the 1σ error ellipse of each high-ionization phase. When the photoionization solution yielded a model N_{ion} for Ne V larger than the measured lower limit value, as is the case for S1, we chose the model N_{ion} for the ratio calculation. The lower limit N_{ion} for Ne V was taken to be the measured lower limit value since it provided a tighter constraint compared to the smallest value obtained from the 1σ error ellipse.

The same process was done for calculating the N_{ion} and errors for Ne VI in S3. The Ne VI column densities for the other outflows are produced in roughly equal amounts from both phases. Assuming the phases are cospatial given the velocity correspondence, they have different n_e values. Therefore, the density cannot be reliably determined from those Ne VI troughs since we would have to deconvolve the troughs into the separate phases. The excited state troughs are all shallower than their resonance counterparts. Therefore, assuming they have the same velocity-dependent covering factors, $C(v)$, and using the maximum values, $C_{\text{max}}(v) = 1 - I_{\text{res}}(v)$ where $I_{\text{res}}(v)$ is the velocity-dependent normalized flux for the resonance trough, the measurements of the excited state column densities are within 30% of their true values, yielding usable density ratios.

In Figure 3, the theoretical column density ratios as a function of n_e are shown with the black contours for each population ratio: dotted = $N(\text{Ne V}^* 569.83 \text{ Å}) / N(\text{Ne V} 568.42 \text{ Å}) = N(\text{Ne V} 413 \text{ cm}^{-1}) / N(\text{Ne V} 0 \text{ cm}^{-1})$, solid = $N(\text{Ne V}^* 572.34 \text{ Å}) / N(\text{Ne V} 568.42 \text{ Å}) = N(\text{Ne V} 1111 \text{ cm}^{-1}) / N(\text{Ne V} 0 \text{ cm}^{-1})$, and dashed = $N(\text{Ne VI}^* 562.81 \text{ Å}) / N(\text{Ne VI} 558.60 \text{ Å}) = N(\text{Ne VI} 1307 \text{ cm}^{-1}) / N(\text{Ne VI} 0 \text{ cm}^{-1})$. The measured column density ratios with uncertainties for each outflow system are overlaid. The different ratios yield consistent n_e within the measurement errors for each outflow system. Therefore, we adopt the $N(\text{Ne V} 1111 \text{ cm}^{-1}) / N(\text{Ne V} 0 \text{ cm}^{-1})$ n_e values for the high-ionization phases since the Ne V* 572.34 Å troughs were the shallowest for each outflow system, yielding the most accurate N_{ion} determinations. The errors for n_e are determined by the horizontal intersection of the ratio including the errors with the CHIANTI curve, e.g., the n_e value where the CHIANTI curve gives the ratio adding the plus error yields the upper error bound on n_e . The n_e for the very high-ionization phases (VHP) are calculated by assuming the two phases are cospatial, and both n_e values are listed in Table 4.

4. Results**4.1. Outflow Distance, Energetics, and Properties**

The distance each outflow is from the central source can be calculated from the definition of the ionization parameter:

$$U_{\text{H}} = \frac{Q_{\text{H}}}{4\pi R^2 n_{\text{H}} c}, \quad (1)$$

where n_{H} is the hydrogen number density with $n_e \approx 1.2n_{\text{H}}$ for highly ionized plasma, R is the distance from the central source, c is the speed of light, and Q_{H} is the incident ionizing photon rate of hydrogen. Integrating the HE0238 SED for energies above 1 Ryd yields $Q_{\text{H}} = 7.3 \times 10^{56} \text{ s}^{-1}$.

The distances of the outflows are given in Table 4, and they are consistent with being located at the same distance within the errors. The small separations in velocity between each outflow also suggests that they are connected. The full width of

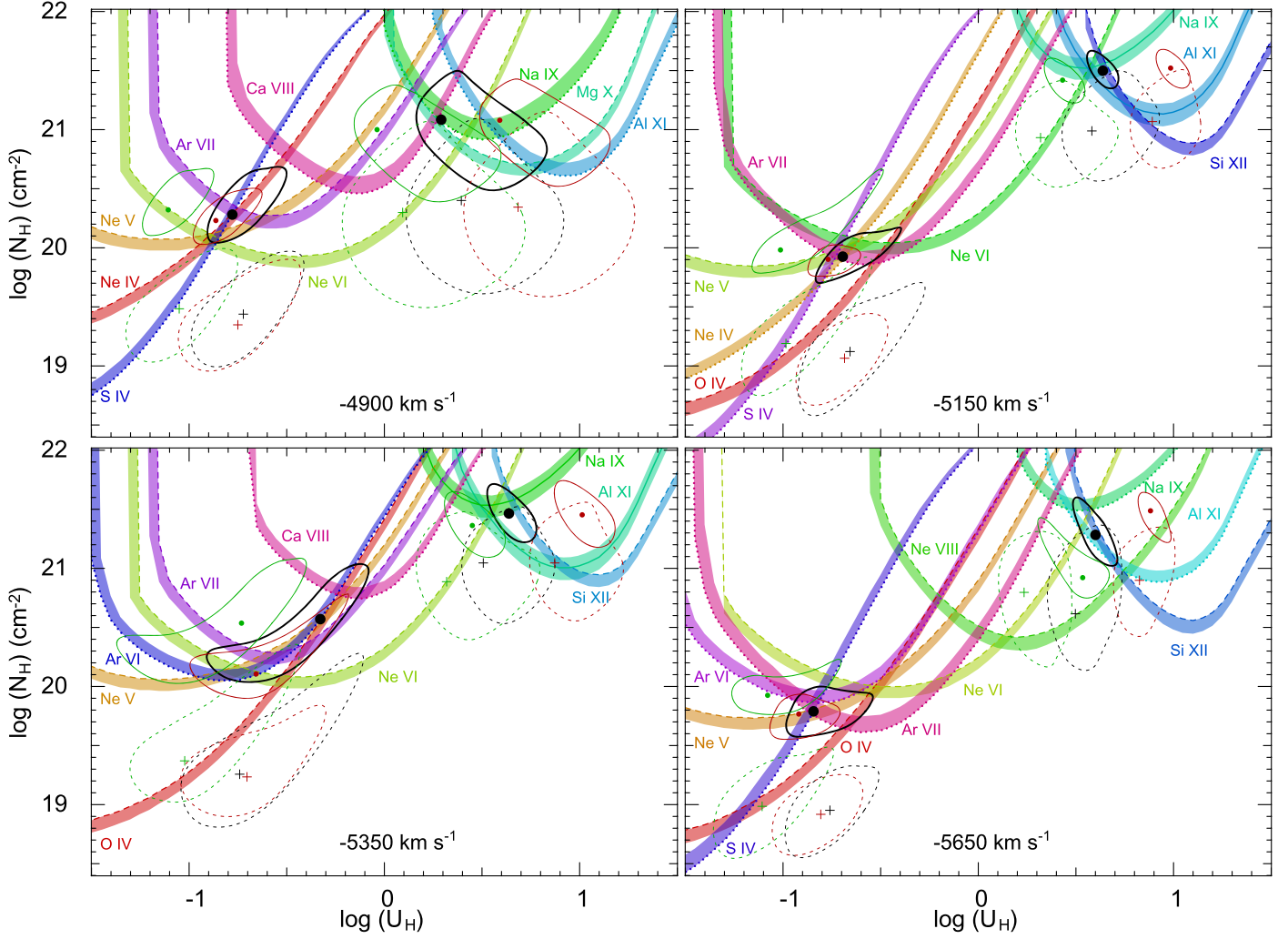


Figure 2. Two-phase photoionization solution for each outflow system. The colored contours show the model parameters that are consistent with the observed values assuming the HE0238 SED and solar metallicity. Solid contours represent ionic column densities taken as measurements, while dotted and dashed contours are upper and lower limits, respectively. The shaded bands are the 1σ uncertainties for each contour (see Table 3). The dots are the best χ^2 -minimization solutions, assuming the solar metallicity for each ionization phase and the ellipses encircling them are their 1σ uncertainties. The black, red, and green solutions are for the HE0238 SED, MF87 SED, and UV-soft SED, respectively. The plus symbol solutions for each phase assume $Z = 4.68 Z_{\odot}$ from Table 3 of Paper V and also account for the same uncertainty in metallicity.

the Ne VIII trough across all outflows is $\sim 1200 \text{ km s}^{-1}$. Using the classification scheme in Section 4.5 of Paper I, the outflows as a whole are a mini-BAL.

Assuming a partially filled thin shell outflow (see Section 5.3 here and Borguet et al. 2012b), the average mass flow rate and kinetic luminosity over the dynamical timescale (R/v) are given by

$$\dot{M} \simeq 4\pi\Omega R N_{\text{H}} \mu m_p v \quad (2)$$

and

$$\dot{E}_{\text{K}} \simeq \frac{1}{2} \dot{M} v^2, \quad (3)$$

where $\Omega = 0.4^{+0.14}_{-0.14}$ is the global covering factor (a fraction of quasars with observed Ne VIII mini-BAL outflows; Muzahid et al. 2013), R is the distance from the central source, $\mu = 1.4$ is the mean atomic mass per proton, N_{H} is the hydrogen column density, m_p is the proton mass, and v is the outflow velocity. Table 4 contains the calculated energetics that are similar for each outflow.

5. Discussion

5.1. Contribution to AGN Feedback

To assess the potential for AGN feedback, Hopkins & Elvis (2010) and Scannapieco & Oh (2004) require kinetic luminosities exceeding 0.5% or 5% of the Eddington luminosity, respectively. Using the Mg II-based black hole mass equation from Bahk et al. (2019) and their methodology to measure the Mg II FWHM and nearby continuum level from Sloan Digital Sky Survey (SDSS) data, the mass of the super massive black hole is $1.0^{+0.9}_{-0.5} \times 10^9 M_{\odot}$ (including systematics) with the corresponding Eddington luminosity (L_{edd}) of $1.3^{+1.1}_{-0.6} \times 10^{47} \text{ erg s}^{-1}$. Each outflow has a kinetic luminosity exceeding the requirement of Hopkins & Elvis (2010) with values above 1.0% of L_{edd} . Collectively, the outflows have a kinetic luminosity of $8.8 \times 10^{45} \text{ erg s}^{-1}$, which is $7.0^{+6.5}_{-2.3}\%$ of L_{edd} . Therefore, these outflows, on average, carry enough energy to contribute substantially to AGN feedback in galaxies with similar black hole masses as in quasar 2MASS J1051+1247. For example, recent theoretical modeling has shown that BAL outflows effectively quench star formation

Table 4
Physical Properties, Distances, and Energetics of the Four Outflow Systems

Outflow System Ionization Phase	S1 = -4900 km s^{-1}		S2 = -5150 km s^{-1}		S3 = -5350 km s^{-1}		S4 = -5650 km s^{-1}	
	Very High	High	Very High	High	Very High	High	Very High	High
$\log(N_{\text{H}})$ (cm^{-2})	$21.08^{+0.41}_{-0.60}$	$20.28^{+0.40}_{-0.23}$	$21.50^{+0.17}_{-0.16}$	$19.93^{+0.24}_{-0.23}$	$21.46^{+0.25}_{-0.24}$	$20.57^{+0.47}_{-0.53}$	$21.28^{+0.32}_{-0.26}$	$19.79^{+0.21}_{-0.22}$
$\log(U_{\text{H}})$ (dex)	$0.3^{+0.5}_{-0.1}$	$-0.8^{+0.3}_{-0.1}$	$0.6^{+0.1}_{-0.1}$	$-0.7^{+0.3}_{-0.2}$	$0.6^{+0.1}_{-0.1}$	$-0.3^{+0.2}_{-0.6}$	$0.6^{+0.1}_{-0.1}$	$-0.8^{+0.3}_{-0.1}$
$\log(n_{\text{e}})$ (cm^{-3})	$^{a}2.8^{+0.3}_{-0.6}$	$3.9^{+0.1}_{-0.3}$	$^{a}2.7^{+0.3}_{-0.3}$	$4.0^{+0.1}_{-0.2}$	$^{a}3.2^{+0.3}_{-0.6}$	$4.2^{+0.1}_{-0.4}$	$^{a}2.5^{+0.4}_{-0.5}$	$3.9^{+0.1}_{-0.2}$
Distance (pc)	460^{+200}_{-130}		360^{+130}_{-100}		180^{+220}_{-50}		460^{+160}_{-140}	
\dot{M} ($M_{\odot} \text{ yr}^{-1}$)	180^{+310}_{-120}		350^{+260}_{-170}		180^{+320}_{-90}		300^{+380}_{-170}	
$\log(\dot{E}_{\text{K}}^{\text{b}})$ (erg s^{-1})	$45.14^{+0.43}_{-0.51}$		$45.46^{+0.25}_{-0.28}$		$45.21^{+0.45}_{-0.51}$		$45.47^{+0.36}_{-0.35}$	
$\dot{E}_{\text{K}}/L_{\text{edd}}$ (%)	$1.1^{+2.4}_{-0.8}$		$2.3^{+3.1}_{-1.4}$		$1.3^{+3.0}_{-0.8}$		$2.3^{+4.4}_{-1.5}$	
$\log(f_{\text{V}})$	$-1.9^{+0.79}_{-0.69}$		$-2.9^{+0.43}_{-0.36}$		$-1.8^{+0.57}_{-0.84}$		$-2.9^{+0.46}_{-0.41}$	

Notes. Bolometric luminosity of $L_{\text{bol}} = 1.3^{+0.1}_{-0.1} \times 10^{47} \text{ erg s}^{-1}$ assuming the HE0238 SED.

^a Assuming that both ionization components are at the same distance.

^b Assuming $\Omega = 0.4$, where N_{H} is the sum of the two ionization phases.

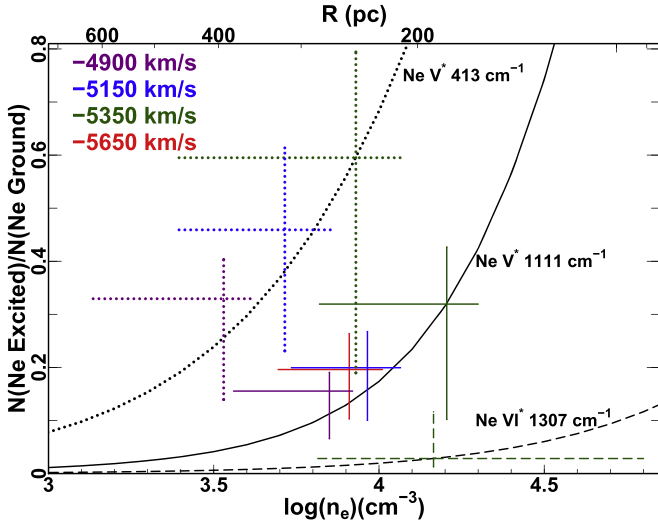


Figure 3. Electron number density, n_{e} , of each outflow system based on three population ratios of Ne. The theoretical predictions from CHIANTI for the population ratios with excited energy levels of $\text{Ne V}^* 413 \text{ cm}^{-1}$, $\text{Ne V}^* 1111 \text{ cm}^{-1}$, and $\text{Ne VI}^* 1307 \text{ cm}^{-1}$ are overlaid. The curves assume the average temperature, 27,500 K, from the photoionization solution for the high-ionization phase of the -5350 km s^{-1} outflow. The corresponding distance, R (from Equation (1)), for this outflow is also shown on the top axis. The offset of the ratios from the shown curves for the other outflows are the result of different electron temperatures given by Cloudy for those outflow systems.

within the host galaxy (e.g., Choi et al. 2018, effective radii up to 10 kpc) and drive gas into the intergalactic medium (e.g., Brennan et al. 2018).

5.2. Photoionization Solution and n_{e} Accuracy

As seen in Figure 2, the photoionization solutions for both phases in S1 and S4, as well as the high phases (HPs) in S2 and

S3, are constrained only by N_{ion} upper and lower limits, which are immune to saturation effects. The multitude of upper and lower limits tightly constrain the errors in the solutions. The photoionization solutions of the HPs determined the upper limits (and sometimes values) of the resonance state N_{ion} for Ne V and Ne VI used to calculate the population ratios that yielded n_{e} for each outflow (see Section 3.3). When multiple diagnostics were available for a given outflow, the n_{e} values were all consistent within errors. This consistency in n_{e} between multiple diagnostics along with the tightly constrained photoionization solutions shows the results are robust and accurate (for more discussions on these issues, see Paper I).

5.3. Geometry and Volume Filling Factor

There are striking similarities in the geometry between outflows. We assume the VHP occupies the space where the outflow resides (Arav et al. 2013). Therefore, the VHPs of S1 and S3 have the same thickness ($N_{\text{H}}/n_{\text{e}}$) of 0.62 pc. Similarly, S2 and S4 have a thickness of 2.0 pc for their VHP. All outflows have thicknesses less than 0.6% of their calculated distances. The similarities continue when looking at the volume filling factor of the HP in each outflow (the VHP volume filling factor = 1 given our assumption). Due to the kinematic similarities of the troughs from the VHP and HP for each outflow, it is physically plausible that the two phases are occupying the same volume. Since the HP is both denser and has a lower N_{H} than that of the VHP, the HP has to have a small volume filling factor within the VHP. This volume filling factor is given by Equation (6) in Paper II (see also Section 2.5 in Paper I):

$$f_{\text{V}} = \frac{U_{\text{H,HP}}}{U_{\text{H,VHP}}} \times \frac{N_{\text{H,HP}}}{N_{\text{H,VHP}}}. \quad (4)$$

S1 and S3 have f_V values differing by 25% without considering errors, and S2 and S4 have the same f_V value (see Table 4). Considering the errors, all four outflows have consistent f_V values. These similarities in geometry, the consistent distances, and small velocity separations suggest the outflows have a common origin.

5.4. Connection to X-Ray Warm Absorbers

The two-phase solutions required for each outflow to sufficiently reproduce the observed N_{ion} from the high- and very high-ionization potential ions are similar to what is seen for X-ray warm absorbers. The ionization parameter of X-ray warm absorbers can span up to five orders of magnitude ($-1 < \log(\xi) < 4$) and necessitate a continuous hydrogen column density as a function of ξ (e.g., Steenbrugge et al. 2003; Costantini et al. 2007; Holczer et al. 2007; McKernan et al. 2007; Behar 2009). The current data allows for higher-ionization phases to exist within the outflows. For the HE0238 SED, $\log(\xi) \approx \log(U_{\text{H}}) + 1.3$, and, therefore, the photoionization solutions are comparable to what is determined for X-ray warm absorbers.

5.5. The “Shading Effect”

Even though the four outflow systems may reside at similar distances, the SED seen by an exterior outflow will be attenuated by an interior one (e.g., Bautista et al. 2010; Sun et al. 2017; Miller et al. 2018). To test the effects this may have on the results, we used the same approach as Miller et al. (2018) and assumed that S3 shades the other outflows since it has the smallest calculated distance and the largest total column density. New Cloudy model grids were generated using the transmitted SEDs from both the high and very high photoionization solutions for S3. New photoionization solutions, distances, and energetics were determined for the other outflows (see elaboration in Paper V). The end result was that the distance and energetics decreased by less than 15%, which is small compared to the overall errors.

6. Summary and Conclusions

This paper presented new *HST*/COS spectra for the quasar 2MASS J1051+1247, which contains four outflow systems. For the first time, we identified absorption troughs from transitions of Ar VI 544.73 Å and 548.90 Å, O IV* 555.26 Å, Ne VI* 562.80 Å, and Ne V* 569.80 Å and 572.30 Å. The absorption troughs yielded ionic column density measurements/lower limits for up to 11 ions in each outflow system. Best-fit photoionization solutions (U_{H} and N_{H}) were determined for each outflow using a grid of photoionization models in conjunction with the ionic column density constraints.

Column density ratios between two excited states and the ground state of Ne V, as well as one excited state and ground state of Ne VI, yielded consistent n_e for the outflows with multiple determinations (see Figure 3). These electron number densities were used in Equation (1) to calculate the distance to the central source of each outflow. The mass flux and kinetic luminosity of each outflow were determined from the distance and Equations (2) and (3). Finally, AGN feedback was assessed, and all of these results are shown in Table 4.

The following emerges from this work:

1. The never-before-seen ionic transitions from Ar VI, O IV*, Ne VI*, and Ne V* were revealed by the EUV500 *HST*/COS observations. The Ne VI* and Ne V* identifications enabled the electron number density, distance, and energetics of all outflows to be determined.
2. A two-phase ionization solution is needed in each outflow to simultaneously satisfy the column density measurements from ions with a wide range of ionization potentials (80–520 eV).
3. The small velocity separations, consistent distances within the errors, and other geometric similarities suggest the outflows originate from the same material at the same distance.
4. The outflows individually (depending on the theoretical work) and collectively have a large enough kinetic luminosity to Eddington luminosity ratio to be major contributors to AGN feedback processes.

T.M., N.A., and X.X. acknowledge support from NASA grants *HST* GO 14777, 14242, 14054, and 14176. This support is provided by NASA through a grant from the Space Telescope Science Institute, which is operated by the Association of Universities for Research in Astronomy, Incorporated, under NASA contract NAS5-26555. T.M. and N.A. also acknowledge support from NASA ADAP 48020 and NSF grant AST 1413319. CHIANTI is a collaborative project involving George Mason University (USA), the University of Michigan (USA), and the University of Cambridge (UK).

ORCID iDs

Timothy R. Miller  <https://orcid.org/0000-0002-0730-2322>
 Nahum Arav  <https://orcid.org/0000-0003-2991-4618>
 Xinfeng Xu  <https://orcid.org/0000-0002-9217-7051>
 Gerard A. Kriss  <https://orcid.org/0000-0002-2180-8266>

References

- Arav, N., Borguet, B., Chamberlain, C., Edmonds, D., & Danforth, C. 2013, *MNRAS*, **436**, 3286
- Arav, N., Chamberlain, C., Kriss, G. A., et al. 2015, *A&A*, **577**, A37
- Arav, N., Liu, G., Xu, X., et al. 2018, *ApJ*, **857**, 60
- Arav, N., Xu, X., Miller, T., Kriss, G. A., & Plesha, R. 2020, *ApJS*, **247**, 37
- Bahk, H., Woo, J.-H., & Park, D. 2019, *ApJ*, **875**, 50
- Bautista, M. A., Dunn, J. P., Arav, N., et al. 2010, *ApJ*, **713**, 25
- Behar, E. 2009, *ApJ*, **703**, 1346
- Borguet, B. C. J., Arav, N., Edmonds, D., Chamberlain, C., & Benn, C. 2013, *ApJ*, **762**, 49
- Borguet, B. C. J., Edmonds, D., Arav, N., Benn, C., & Chamberlain, C. 2012a, *ApJ*, **758**, 69
- Borguet, B. C. J., Edmonds, D., Arav, N., Dunn, J., & Kriss, G. A. 2012b, *ApJ*, **751**, 107
- Brennan, R., Choi, E., Somerville, R. S., et al. 2018, *ApJ*, **860**, 14
- Chamberlain, C., & Arav, N. 2015, *MNRAS*, **454**, 675
- Choi, E., Somerville, R. S., Ostriker, J. P., et al. 2018, *ApJ*, **866**, 91
- Costantini, E., Kaastra, J. S., Arav, N., et al. 2007, *A&A*, **461**, 121
- Crenshaw, D. M., Kraemer, S. B., & George, I. M. 2003, *ARA&A*, **41**, 117
- Dai, X., Shankar, F., & Sivakoff, G. R. 2008, *ApJ*, **672**, 108
- de Kool, M., Arav, N., Becker, R. H., et al. 2001, *ApJ*, **548**, 609
- de Kool, M., Becker, R. H., Arav, N., Gregg, M. D., & White, R. L. 2002, *ApJ*, **570**, 514
- Dere, K. P., Landi, E., Mason, H. E., Monsignori Fossi, B. C., & Young, P. R. 1997, *A&AS*, **125**, 149
- Dunn, J. P., Bautista, M., Arav, N., et al. 2010, *ApJ*, **709**, 611
- Ferland, G. J., Chatzikos, M., Guzmán, F., et al. 2017, *RMxAA*, **53**, 385

- Ganguly, R., & Brotherton, M. S. 2008, [ApJ](#), **672**, 102
- Green, J. C., Froning, C. S., Osterman, S., et al. 2012, [ApJ](#), **744**, 60
- Grevesse, N., Asplund, M., Sauval, A. J., & Scott, P. 2010, [Ap&SS](#), **328**, 179
- Hamann, F. W., Barlow, T. A., Chaffee, F. C., Foltz, C. B., & Weymann, R. J. 2001, [ApJ](#), **550**, 142
- Hewett, P. C., & Foltz, C. B. 2003, [AJ](#), **125**, 1784
- Holczer, T., Behar, E., & Kaspi, S. 2007, [ApJ](#), **663**, 799
- Hopkins, P. F., & Elvis, M. 2010, [MNRAS](#), **401**, 7
- Kaasta, J. S., Kriss, G. A., Cappi, M., et al. 2014, [Sci](#), **345**, 64
- Kaasta, J. S., Mewe, R., Liedahl, D. A., et al. 2000, [A&A](#), **354**, L83
- Knigge, C., Scaringi, S., Goad, M. R., & Cottis, C. E. 2008, [MNRAS](#), **386**, 1426
- Korista, K. T., Bautista, M. A., Arav, N., et al. 2008, [ApJ](#), **688**, 108
- Landi, E., Young, P. R., Dere, K. P., Del Zanna, G., & Mason, H. E. 2013, [ApJ](#), **763**, 86
- Mathews, W. G., & Ferland, G. J. 1987, [ApJ](#), **323**, 456
- McKernan, B., Yaqoob, T., & Reynolds, C. S. 2007, [MNRAS](#), **379**, 1359
- Miller, T. R., Arav, N., Xu, X., et al. 2018, [ApJ](#), **865**, 90
- Miller, T. R., Arav, N., Miller, T., Kriss, G. A., & Plesha, R. 2020, [ApJS](#), **247**, 41
- Moe, M., Arav, N., Bautista, M. A., & Korista, K. T. 2009, [ApJ](#), **706**, 525
- Murray, N., Chiang, J., Grossman, S. A., & Voit, G. M. 1995, [ApJ](#), **451**, 498
- Muzahid, S., Srianand, R., Arav, N., et al. 2013, [MNRAS](#), **431**, 2885
- Proga, D., & Kallman, T. R. 2004, [ApJ](#), **616**, 688
- Proga, D., Stone, J. M., & Kallman, T. R. 2000, [ApJ](#), **543**, 686
- Reynolds, C. S. 1997, [MNRAS](#), **286**, 513
- Scannapieco, E., & Oh, S. P. 2004, [ApJ](#), **608**, 62
- Schlafly, E. F., & Finkbeiner, D. P. 2011, [ApJ](#), **737**, 103
- Steenbrugge, K. C., Kaastra, J. S., de Vries, C. P., et al. 2003, [A&A](#), **402**, 477
- Sun, L., Zhou, H., Ji, T., et al. 2017, [ApJ](#), **838**, 88
- Wright, E. L. 2006, [PASP](#), **118**, 1711
- Xu, X., Arav, N., Miller, T., et al. 2019, [ApJ](#), **876**, 105
- Xu, X., Arav, N., Miller, T., & Benn, C. 2018, [ApJ](#), **858**, 39
- Xu, X., Arav, N., Miller, T., Kriss, G. A., & Plesha, R. 2020a, [ApJS](#), **247**, 38
- Xu, X., Arav, N., Miller, T., Kriss, G. A., & Plesha, R. 2020b, [ApJS](#), **247**, 40
- Xu, X., Arav, N., Miller, T., Kriss, G. A., & Plesha, R. 2020c, [ApJS](#), **247**, 42